WILEY-VCH

Laser-induced Electron Synchronization Excitation for Photochemical Synthesis and Patterning Graphene-based Electrode

Yongjiu Yuan[a,b,c,d], *Junhao Huang*[a,b,c], *Xin Li*[*,a,b,c], *Lan Jiang*[a,b,c], *Tong Li*[d], *Pengcheng Sun*[d], *Yingying Yin*[d], *Sumei Wang*[a,b,c], *Qian Cheng*[a,b,c], *Wanghuai Xu*[d,e], *Liangti Qu*[f], *Steven Wang*[d]

a. Laser Micro/Nano-Fabrication Laboratory, School of Mechanical Engineering, Beijing Institute of Technology, Beijing, 10081, China.

b. Yangtze Delta Region Academy of Beijing Institute of Technology, Jiaxing, 314000, China.

c. Beijing Institute of Technology Chongqing Innovation Center, Chongqing, 401120, China.

d. Department of Mechanical Engineering, City University of Hong Kong, Hong Kong, 999077, China.

e. Department of Mechanical Engineering, The Hong Kong Polytechnic University, Hong Kong, 999077, China

f. MOE Key Laboratory of Bioorganic Phosphorus Chemistry & Chemical Biology, Department of Chemistry, Tsinghua University, Beijing, 100084, China.

*Corresponding author email: lixin02@bit.edu.cn

Abstract

Micro-supercapacitors (MSCs) represent a pressing requirement for powering the forthcoming generation of micro-electronic devices. The simultaneous realization of high-efficiency synthesis of electrode materials and precision patterning for MSCs in a single step presents an ardent need, yet it poses a formidable challenge. Herein, a unique shaped laser-induced patterned electron synchronization excitation strategy has been put forward to photochemical synthesis RuO_2/rGO electrode and simultaneously manufacture the micron-scale high-performance MSCs with ultra-high resolution. Significantly, our technique represents a noteworthy advancement over traditional laser direct writing (LDW) patterning and photoinduced synthetic electrode methods. It not only improves the processing efficiency for MSCs and the controllability of laser-induced electrode material but also enhances electric fields and potentials at the interface for better electrochemical performance. The resultant MSCs exhibited excellent area and volumetric capacitance (516 mF cm^{-2} and 1720 F cm^{-3}), and ultrahigh energy density (0.41 Wh cm^{-3}) and well-cycle stability (retaining 95% capacitance after 12,000 cycles). This investigation establishes a novel avenue for electrode design and underscores substantial potential in the fabrication of diverse microelectronic devices.

Keywords: laser, graphene, photochemical synthesis, supercapacitors

1. Introduction

The rapid proliferation of micro portable electronic devices has brought increased prominence to micro energy storage devices.[1-3] While diminutive lithium-ion batteries are presently the prevailing choice, their restricted power density renders them insufficient for diverse practical applications. Conversely, conventional capacitors offer elevated power density but exhibit limited energy density. Micro-supercapacitors (MSCs) represent an intermediate energy storage solution between micro batteries and conventional capacitors. MSCs offer heightened energy density compared to traditional capacitors, superior power density when compared to batteries, and demonstrate exceptional cycle life exceeding 10^5 cycles, while also facilitating ultra-fast charging and discharging processes.[4-6] In terms of their energy storage mechanisms, MSCs are categorized into two primary classes: electrical double layer capacitors (EDLCs) and pseudocapacitors. EDLCs store and release charge via ion adsorption and desorption at the electrode surface, a process contingent on the high specific surface area of the active material, exemplified by materials like activated carbon and graphene. In contrast, pseudocapacitors rely on reversible Faraday reactions within pseudocapacitive electrode materials, thus affording them higher energy density potential. However, the limited stability of pseudocapacitive materials across charge/discharge cycles can undermine their cycle life. This degradation results from the structural integrity and electrochemical behavior of the pseudocapacitive material being compromised during the charging and discharging processes, thereby impinging upon the lifetime of pseudocapacitors.[7-9]

In recent times, a multitude of studies have focused on amalgamating pseudocapacitive materials with double-layer materials to fabricate composite electrodes, thereby realizing high-performance energy storage solutions. For instance, research endeavors involving the combination of graphene with metal oxides,[10-12] metal sulfides,[13,14] polymeric materials[15,16] and more, to form composite electrode materials, have been continuously reported. Graphene, as an exceptional two-dimensional material, not only embodies the aforementioned advantages but also presents the potential for fabricating flexible energy storage devices due to its exceptional mechanical properties. Furthermore, with its exceptionally high theoretical capacitance values, prolonged cycle life, and an extensive potential window, ruthenium oxide stands out as one of the most auspicious pseudocapacitive materials[17-19]. Ruthenium oxide endows energy storage systems with remarkable capacity via rapid and reversible redox reactions. Meanwhile, two-dimensional materials serve to maintain robust power densities by acting as efficient conducting networks. Additionally, their electrochemical properties contribute to an extended cycle life and elevated electrical conductivity.[20-22] In light of these attributes, the combination of graphene

and RuO_2 offers the promise of constituting a well-rounded composite electrode material, capable of delivering comprehensive performance across multiple dimensions.

In addition to the necessity for well-designed electrode materials, it is imperative to develop a technology that can realize the synthesis of electrode materials and the fabrication of complete MSCs at high resolutions. Currently, several established methods for MSC fabrication, including electrodeposition, wet chemical synthesis, and chemical vapor deposition and so on.[23-27] Nevertheless, for microdevices requiring high resolution, these methods face challenges in achieving high-quality patterning and selective control over material synthesis. LDW offers distinct advantages as a one-step, straightforward, and efficient method, facilitating the patterning of MSC electrodes in various shapes while concurrently synthesizing hybrid electrode materials.[28-30] However, despite its merits, the direct laser writing approach is incapable of fabricating the entire electrode material for MSCs simultaneously. Additionally, its precision is constrained by the laser spot size, rendering it insufficient for addressing the requirements of high precision and consistency in microelectronic device preparation necessitated by the quest for greater efficiency.

Here, we directly patterned micron-sized and high precision MSCs morphology and synthesize reduced graphene oxide (rGO)/RuO_2 materials in one step by means of a spatially shaped femtosecond laser-induced electron synchronization excitation. Leveraging this streamlined technique, the efficiency of fabricating the MSCs has reached over 30,000 within a mere 10-minute span. The resultant SSL-induced MSCs are sized within tens of micrometers (20×20 μm²). The rGO/RuO_2 was successfully prepared by photochemically synthesis the Ru^{3+} in ruthenium chloride to Ru^{4+} by means of femtosecond laser while removing the oxygens from GO. The three-dimensional porous architecture of rGO offers a platform for the immobilization of ruthenium oxide nanoparticles, where said nanoparticles become affixed to the nanosheets of rGO. These interactions involve oxidative and reductive processes, respectively. During the oxygenation and deoxygenation steps, the photoinduced synthesis reactions of the two electrode materials synergistically enhance one another. Ruthenium oxide contributes to the high capacitance through a rapid and reversible redox reaction, while the mechanical resilience and stability of the rGO nanosheets confer an extended cycle life to the manufactured MSCs. The rGO/RuO_2 MSCs prepared by spatially shaped laser (SSL) has an area capacitance of 516 mF cm^{-2} and a volume capacitance value of 1720 F cm^{-3}. The capacitance retention of the capacitors was ~95% after 12,000 charge/discharge circles with different voltage windows, benefiting from the stability of rGO as carbon-based electrode material. To substantiate the efficacy of employing spatially shaped femtosecond laser technology in the synthesis of electrode materials,

we conducted a comparative analysis by employing the femtosecond laser direct writing method to fabricate rGO/RuO_2 composites. Our findings reveal superior electrochemical performance metrics for the electrode materials generated via SSL as opposed to those synthesized using the laser direct writing approach. Specifically, the outcomes indicate that laser direct writing leads to the inadvertent removal of the graphene layer, a consequence of the movement of the Gaussian pulse, concomitantly resulting in the unintentional elimination of RuO_2 nanoparticles. This SSL approach, conversely, obviates the milling-like phenomenon arising from the motion of the laser pulses, rendering it a more efficient and ensuring enhanced surface uniformity when juxtaposed with the laser direct writing technique.

2. Results and Discussion

2.1. Manufactured technology for rGO/RuO_2 MSCs

As shown in Figure 1a, a spatial light modulator (SLM) is used to directly shape the light field. The electrode shape was designed to determine the intensity distribution by positioning the 256×256-pixel region to a black 1080×1920 background image. Furthermore, the algorithm has been fine-tuned using an improved Gerchberg-Saxton algorithm, which involves augmenting the number of iterations and employing a distance optimization function to refine the arrangement of beam points. Subsequently, the grayscale phase hologram is uploaded onto the SLM to manipulate the light field associated with diverse geometric shapes. Supplementary Figure 1 illustrates the complete optical pathway of the SSL system. The initial Gaussian laser beam undergoes spatial modulation via the SLM, is further guided through two plane-convex lenses, and ultimately converges at the 20× objective lens.

Ultimately, the process culminates in focusing on the sample surface to achieve complete pattern manufacturing. Figure 1a provides a visual representation of the traditional LDW method, which involves cumulative point-by-point scanning for patterning. It becomes evident that SSL technology enables one-step, instantaneous processing of patterned electrode structures, allowing for the simultaneous reduction and oxidation of the entire composite electrode material. The SSL technology can complete a complete micro supercapacitor pattern processing with a single pulse, its processing efficiency can reach 4,000 micro supercapacitors per minute, nearly 500 times higher than LDW processing efficiency.

The chemical equation for the photoinduced synthesis of the composite electrode material is also depicted in Figure 1a, with a more detailed illustration available in Supplementary Figure 2. LDW gradually completes the entire process of patterning and photoinduced electrode synthesis through point-to-point superposition and accumulation. In this process, the overlap of

focused light spots between the front and back can lead to the subsequent pulse erasing a portion of the electrode material created by the preceding pulse.

In contrast, SSL technology adeptly circumvents these issues by simultaneously achieving pattern processing across time and space dimensions. Supplementary Figure 3 features an animation illustrating the patterned MSCs processing using both SSL and LDW, offering an intuitive portrayal of SSL's efficient one-step patterning capability. Even when the LDW method is limited to processing relatively simple patterns (such as straight shapes), it substantially lags behind SSL technology when it comes to processing complex patterns. Supplementary Figure 4 further highlights the distinctions between traditional Gaussian laser point-by-point scanning and SSL projection processing in the induction of materials.

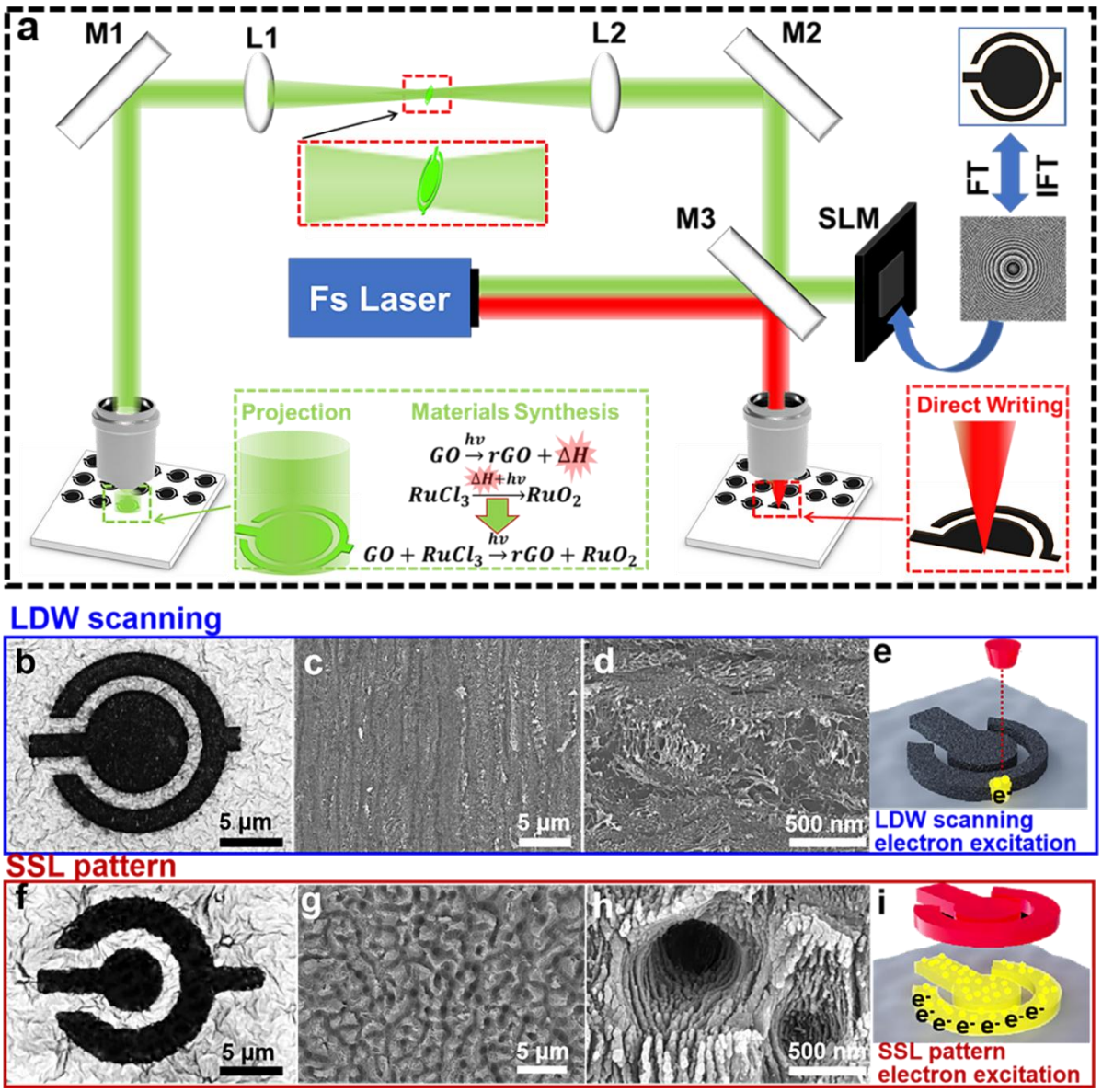

Figure 1. LDW scanning and SSL excitation of MSCs and the surface morphology of photoinduced composite electrode. (a) The schematic diagram of SSF and LDW processing of

MSCs. (b) The characterization of rGO/RuO_2 by Laser Direct Writing (rGO/RuO_2–LDW). (c) Low and high (d) magnification SEM images of rGO/RuO_2-LDW. (e) The electron excitation mechanism of LDW regulating materials. (f) The characterization of rGO/RuO_2 by SSL (rGO/RuO_2–SSL). (g) Low and (h) high magnification SEM images of rGO/RuO_2-SSL. (i) The electron excitation mechanism of SSL regulating materials.

The rGO/RuO_2 patterned MSCs prepared by LDW method (rGO/RuO_2-LDW) and the SSL (rGO/RuO_2-SSL) are shown in Figure 1 b-i. The characterization in Figure 1b and f show that two strategies can both produce a well-formed MSCs patterns. The dimensions of the entire electrode assembly do not exceed 20×20 μm^2, allowing for the realization of exceptionally high-precision micro and nano processing. Nonetheless, our SSL technology offers the capability to produce larger microelectrodes by adjusting the size of the designed optical field and broadening the beam. Supplementary Figure 5 presents a spectrum of patterned electrodes of varied sizes, all fabricated through the SSL single-pulse one-step method, encompassing rGO/RuO_2 electrode dimensions ranging from 15×15 μm^2 to 300×300 μm^2. Furthermore, the SSL technology can be adeptly employed for the patterning of electrodes in diverse shapes. By means of customized light field shaping and control, personalized electrode patterns can be meticulously created, as depicted in Supplementary Figure 6, which showcases an array of distinct shapes for rGO/RuO_2 electrode patterns fashioned using SSL technology. Supplementary Figure 7 shows scanning electron microscope (SEM) images of the surface of the material after laser patterned processing and raw processing. The laser-induced micro-nano porous structure of the surface can be clearly found. The surface structures of rGO/RuO_2-LDW and rGO/RuO_2-SSL are shown in Figure 1c and g. The surface structure of the rGO/RuO_2-LDW shows irregular surface lamellar protrusions, while the surface structure of rGO/RuO_2-SSL has a groove-like structure and holes, which increases the surface area and facilitates the penetration and transport of electrolyte. The production of RuO_2 nanoparticles during SSL processing can be observed in Supplementary Figure 8. Through the locally enlarged SEM image, we can measure the diameter of these nanoparticles between 3 and 5 nanometers. These nanoparticles are distributed on the surface of the layered nanostructure, which adds more active sites to the composite and increases its specific surface area. In order to further investigate the differences between the LDW and SSL, microscopic characterization of rGO/RuO_2 under different laser pulse energy processed by both methods are shown in Supplementary Figure 9. Supplementary Figure 9a indicates the surface structure of rGO/RuO_2-LDW under different laser pulse energy. It can be seen that the surface of rGO/RuO_2-LDW is an irregular lamellar structure with a small number of ruthenium oxide nanoparticles. With an elevation in laser pulse energy, there is a

discernible escalation in the surface lamellar structures. However, simultaneously, the dimensions of these lamellae exhibit a reduction. Furthermore, as the laser pulse energy is raised, there is an observed proliferation in the surface pores of rGO/RuO_2-LDW. This suggests that the augmented laser pulse energy results in the deterioration of the reduced graphene oxide sheets on the surface and consequent removal of the electrode material. Supplementary Figure 9b shows the surface structure of rGO/RuO_2-SSL at different laser pulse energy. In contrast to rGO/RuO_2-LDW, the surface structure of rGO/RuO_2-SSL exhibits a distinctive gully-like configuration. At lower laser pulse energy levels, the surface of rGO/RuO_2-SSL remains relatively smooth, with minimal protrusions and a scarcity of ruthenium oxide nanoparticles. As the laser pulse energy is incrementally raised, the groove-like protrusions become more pronounced, and an increased quantity of nanoparticles becomes evident, firmly adhering to the surface of rGO sheets. Elevating the laser pulse energy leads to the formation of deeper laser ablation pits on the surface, yet concurrently, the nanoparticles surrounding these pits are removed as a consequence of rGO sheet removal.

Consequently, we tentatively conclude that the rGO/RuO_2-SSL has an excellent conforming surface structure, due to the advantages of the spatially shaped femtosecond laser to fabricate the entire micro-supercapacitor in one step. The SSL is also able to avoid the milling-like phenomenon of rGO/RuO_2 caused by the movement of the laser pulses in the laser direct writing method. Supplementary Figure 10 shows the pattern of the composite rGO hybrid electrode induced by SSL. The apparent distribution of Ru, O and C elements can be seen, which proves the synthesis of the composite electrode material during the processing. As depicted in Figure 1e, in the case of LDW, the laser spot scans points by point, sequentially interacting with the material over time. At any given moment, only a single point experiences instantaneous electron excitation. In contrast, with the SSL technology (as illustrated in Figure 1i), the entire pattern is instantaneously subjected to electron excitation. This variance in the number of excited electrons at any given moment directly influences material modification and, consequently, the subsequent charge and ion conduction processes.

2.2 Mechanism and characterization of laser-induced synthesis of rGO/RuO_2.

The femtosecond (10^{-15} second) laser we use in our experiments is an ultra-fast laser with a pulse width of femtosecond magnitude. In this process, photons transfer energy to electrons, whose heating promotes interband transitions, leading to collision ionization and avalanche ionization. Since the time scale of a material's phase transition is about nanoseconds (10^{-9} second), femtosecond lasers can control the reduction and modification of materials by

adjusting the electron density prior to the phase transition.[31-33] In Figure 2a, the diagram illustrates the progression and specific stages of photoinduced material synthesis, denoting the associated time scales. When the femtosecond laser reaches the surface of the material, the excited free-moving electrons become active for (10^{-15}~10^{-12}s), causing further absorption of energy and inducing lattice changes. In our work, this process is embodied in the photochemical reduction of graphene oxide, a process in which oxygen is lost, accompanied by ionization of electrons. Then Ru^{3+} in the material will absorb oxygen and oxidize under the action of electron and photoinduced energy to form a new oxide. The two reactions happen to promote each other, so a new mixture (rGO/RuO_2) is created, along with the evaporation of excess gas and water vapor.

The enormous instantaneous power of SSL can disrupt carbon-oxygen chemical bonds, thereby reducing GO to rGO. Simultaneously, SSL provides a substantial number of excited photons, creating free-moving electrons and holes. Under their influence, the electron transfer process is intensified. With an increase in laser energy, the resulting thermal effects also promote further reduction of GO to rGO. At the same time, the electrons of Ru^{3+} undergo a transition from the ground state to a highly excited state. In this highly excited state, Ru^{3+} possess sufficient energy to react with the surrounding oxygen. Due to its higher oxidation potential, Ru^{3+} can utilize anchoring points provided by graphene oxide for oxidation, converting Ru^{3+} from a lower oxidation state to RuO_2.

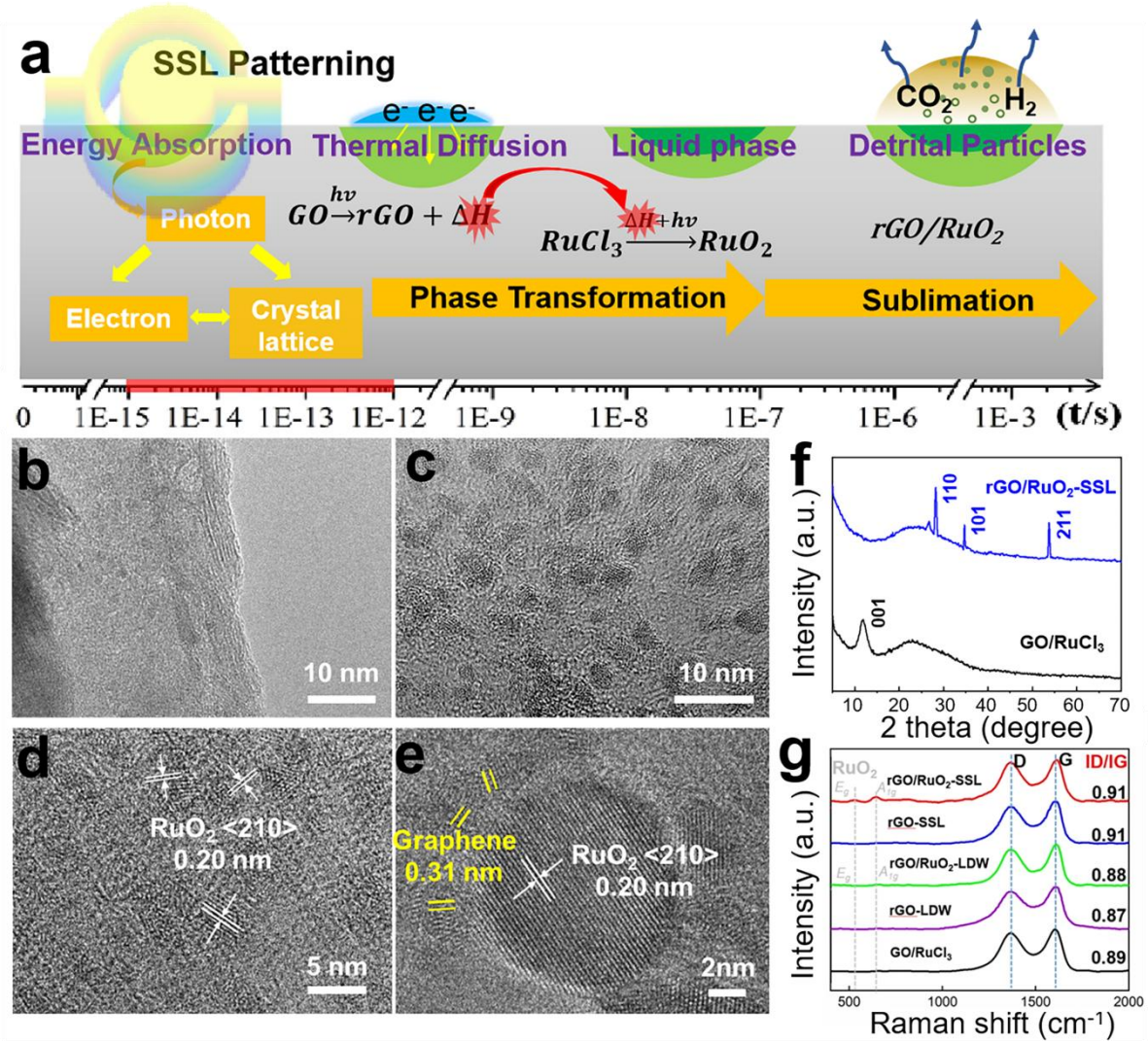

Figure 2. The laser-induced synthesis mechanism and characterization of composite electrode materials. (a) The schematic of the resultant morphology changes and phase transformation by SSL under the proposed photochemical routes. (b-e) TEM images of rGO/RuO_2–SSL under different magnifications illustrating that the RuO_2 nanoparticles are wrapped by rGO sheets. (f) X-ray diffraction (XRD) patterns of the composite material. (g) Raman spectra of the composite materials.

Figure 2b-e show TEM images of rGO/RuO_2 –SSL under different magnifications. In Figure 2b, the two-dimensional layered structure is distinctly visible along the edges, with elliptical nanoparticles of different materials observed on this layered structure. The average size of the RuO_2 nanoparticles in Figure 2c is 3~5 nm. The spacing of the nanoparticles measured in Figure 2d and e is 0.20 nm, which is consistent with the <210> d-spacing of RuO_2 nanoparticles. Therefore, the spatially shaped femtosecond laser method can successfully obtain reduced graphene oxide lamellae attached to RuO_2 nanoparticles.[34,35] The rGO lamellae can provide attachment sites for RuO_2 nanoparticles, providing good mechanical properties and

ensuring the structural stability of the composite. The ripple-like wrinkled structure of graphene can improve the electrochemical performance of devices50, and the lattice space of 0.31 nm (Figure 2e) corresponds to the distance between two neighboring (002) planes in graphitic materials. The rGO flakes have a high specific surface area, ensuring excellent ion transport and allowing the RuO_2 nanoparticles as electrode to be in full contact with the electrolyte, thus obtaining excellent capacitive. Supplementary Figure 11 shows the TEM-EDS elemental mapping of rGO/RuO_2-SSL sample with the elemental distribution of C, O, and Ru. The X-ray diffraction (XRD) patterns of the as-prepared rGO/RuO_2-SSL nanocomposite and original GO/$RuCl_3$ are presented in Figure 2f. The peak of GO at 2θ =11.2° corresponds to the (001) reflection in GO/$RuCl_3$. The presence of RuO_2 in the composites is confirmed by the characteristic diffraction peaks of the RuO_2 (110), (101) and (211) planes at 2θ values of around 28.2, 34.6, 53.7, respectively, (JCPDS 40-1290, 43-1027).[36,37] The Raman spectra of the rGO/RuO_2-SSL, rGO-SSL, rGO/RuO_2-LDW, rGO-LDW and GO/$RuCl_3$ materials are shown in Figure 2g. The initial materials has a wide band at 1350 cm^{-1} of D-band and 1588 cm^{-1} of G-band respectively, while the rGO reduced by femtosecond laser had two peaks at the same position with the nearly same height, which was consistent with the previous research. The ratio of intensity at D-band relative to intensity at G-band, ID/IG, was shown in the figure. The change in the intensity of the two peaks can account for the transformation of the untreated GO surface from the sp^3 conformation characteristic to the sp^2 geometry characteristic of graphene-like structure. According to the Raman spectra range of 450–800 cm^{-1}, rGO/RuO_2-SSL and rGO/RuO_2-LDW composites exhibited two peaks located at 525 and 637 cm^{-1} related to the E_g mode and A_{1g} mode group vibrations of RuO_2.[38,39] A partial magnification of this Raman spectra can be seen in supplementary Figure 12. Supplementary Figure 13 shows the ID/IG of rGO/RuO_2-SSL and rGO/RuO_2-LDW at different laser pulse energy. The D and G peak positions of rGO/RuO_2-SSL exhibit a discernible blue shift when compared to those of rGO/RuO_2-LDW, which suggests the nanopores in rGO/RuO_2-SSL influences the vibrational modes of molecules. This porous structure tends to cause some defects due to its multi-interface surface and high-energy sites, which can increase the ion diffusion rate and furnishing more active sites for chemical reactions in electrochemical energy storage. The ID/IG ratio was highest, reaching 0.93, when the laser pulse energy of SSL was 60 μW.

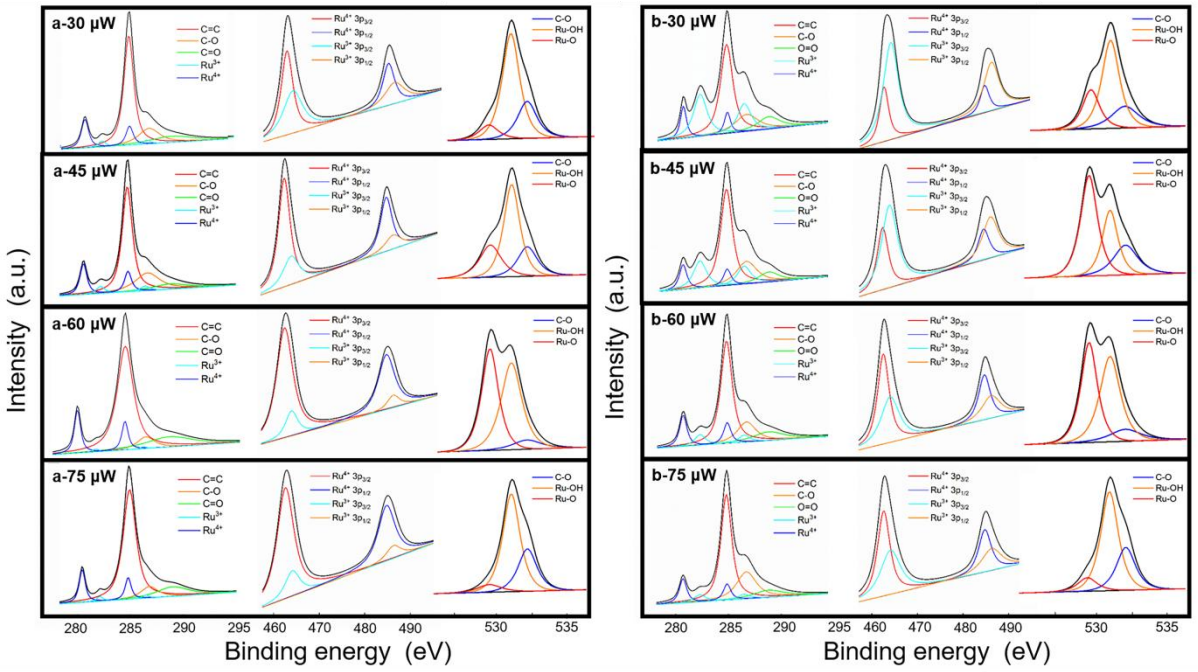

Figure 3. The X-ray photoelectron spectroscopy (XPS) spectra of C 1s, Ru 3p and O 1s. (a) The high-resolution XPS spectra rGO/RuO_2-SSL and (b) rGO/RuO_2-LDW materials under different laser pulse energy.

The XPS spectra of rGO/RuO_2–SSL and rGO/RuO_2–LDW at different laser pulse energy are shown in Figure 3. The XPS spectra of C 1s, Ru 3p and O 1s of the original GO/$RuCl_3$ film is shown in Supplementary Figure 14. In the process of laser induced GO/$RuCl_3$ photochemical reaction, the laser pulse energy will be affected. We synthesized rGO/RuO_2 electrodes by using a stepped-up laser energy (30-75 μw), and characterized both rGO/RuO_2-SSL and rGO/RuO_2-LDW XPS spectra. By fitting the spectra of rGO as well as RuO_2, it's possible to find out whether the oxygens on the surface of graphene oxide are removed and the Ru^{3+} in ruthenium chloride is oxidised to Ru^{4+} in RuO_2. Figures 3a and 3b indicate the photoemission peaks of the Ru^{4+} 3p3/2 and 3p1/2 at 484.8 eV and 462.6 eV respectively, while the photoemission peaks of the Ru^{3+} 3p3/2 and 3p1/2 are at 486.3 eV and 464.1 eV respectively (the 3p spin-orbit splitting is 22.2 eV). A distinct C 1s peak is observed at 284.8 eV, where the 3d peaks of Ru are also present. Besides, the Ru 3d5/2 photoemission peaks are observed at 280.7eV and 282.2 eV, corresponding to +4 and +3 Ru cations, respectively. The highest peak corresponds to C1s peak at 284.8 eV, and there are C-O at 286.7 eV and C=O at 288.9 eV, corresponding to GO.[40-42] The peak at 529.7 eV with was ascribed to Ru-O-Ru and other two peaks at 531.2 eV and 532.3 eV were resulted from Ru-OH and the C-O. As can be seen in Figure 3, with the intensity of the C-O and C=O peaks decreasing as the laser pulse energy increases, and the oxygens groups on the graphene oxide surface are further removed. Compared to the rGO/RuO_2–LDW, the

intensity of the C-O and C=O peaks are weaker in the rGO/RuO_2–SSL.

The table summarizes the XPS data for the C 1s, O 1s and Ru 3p peaks in Figure 3. From the data in the Table, it presents the characteristic peaks and corresponding percentages of C 1s, O 1s, Ru^{3+}, and Ru^{4+}. In our original material GO/$RuCl_3$, the ratio of Ru^{3+} is high, while the ratio of C/O is close to 2:1. As the laser REDOX the original material, the proportions of the elements change. When the laser energy increases gradually, the proportion of Ru^{4+} increases gradually, while the proportion of Ru^{3+} decreases gradually, suggesting the generation of RuO_2. When the energy of SSL and LDW reaches 60 μW and 75 μW, the ratio of Ru^{4+} decreases.

Our analysis indicates that the substantial laser energy employed leads to the direct removal of the laser-induced modified material. As a result, the analyzed material represents a composite product consisting of the original material and a portion of the laser-induced material. We analyzed that under this laser parameter, SSL has the best oxidation effect on $RuCl_3$ and the highest RuO_2 content. Additionally, the proportion of tetravalent ruthenium in rGO/RuO_2-SSL significantly surpasses that in rGO/RuO_2-LDW. This observation suggests that the SSL technology can circumvent material removal issues arising from the Gaussian laser spot movement encountered in LDW method, thus ensuring the consistency of the rGO/RuO_2 material.

Furthermore, a detailed analysis of the C/O ratios in the laser-induced products was conducted. The C/O ratio serves as an indicator of the extent of graphene reduction. The oxygen component in the analysis encompasses oxygen associated with RuO_2 and graphene due to the formation of metal oxides during the laser-induced synthesis of the material. By calculating the oxygen ratio in different components based on the RuO_2 content, we were able to determine the C/O ratio, offering insight into the degree of graphene reduction. When the laser energy of SSL is 60 μW, the resulting graphene has the C/O ratio of 35.04, which is much higher than the C/O ratio of LDW processed graphene. The C/O ratio of SSL-induced reduced graphene was 17.5 times higher than that of the original GO material, which fully demonstrated the outstanding reduction capability of SSL technology for GO.

Table 1. Summary of the XPS for GO/$RuCl_3$ and rGO/RuO_2 induced by SSL and LDW.

Material	Laser pulse energy (μW)	C 1s	O 1s		Ru^{3+} 3p	Ru^{4+} 3p
			O 1s (associated with graphene)	O 1s (associated with RuO_2)		
GO/$RuCl_3$	-	60.45%	27.58%	0.86%	11.54%	0.43%

rGO/RuO_2 –SSL	a-30	65.78%	21.81%	1.56%	10.07%	0.78%
	a-45	73.79%	10.70%	7.98%	3.54%	3.99%
	a-60	75.34%	2.15%	14.14%	1.30%	7.07%
	a-75	62.57%	23.82%	5.80%	4.91%	2.90%
rGO/RuO_2 –LDW	b-30	70.12%	9.78%	10.30%	4.65%	5.15%
	b-45	73.23%	6.19%	11.38%	3.51%	5.69%
	b-60	74.68%	4.54%	11.9%	2.93%	5.95%
	b-75	61.09%	16.59%	9.52%	8.04%	4.76%

To delve deeper into the disparities between LDW and SSL with regard to laser processing and the synthesis of composite electrode materials, the processing was meticulously scrutinized using pump-probe technology. As shown in Figure 4a, SSL and LDW are observed with a processing light and a probe light, in which the pulse flux is both 0.3 J cm^{-2}. Figure 4b and c show the morphology of SSL and LDW ablation on the sample surface. The processing area of SSL is significantly larger than that of LDW. Figure 4d-g shows the observation of SSL and LDW laser processing under different pulse delays. It can be seen from the figure that SSL can be significantly observed, while LDW needs to be barely observed with a time delay of 100 ps. This observation underscores the disparities in plasma eruption intensity resulting from the interaction of materials with different lasers. It directly underscores that, under identical conditions, the processing efficacy of SSL is markedly superior to that of LDW.

Figure 4h and i is the simulation diagram of the electric field and potential when LDW and SSL are processed as patterned electrode materials by COMSOL software. We can clearly see that the electric field intensity at the end of point-by-point processing (upper right) is much larger than that in other positions, indicating the electric field of the laser focused region is active and the intensity of the electric field declines gradually in other regions. The electric field intensity in SSL is strong and uniform. The same goes for the strength of the electric potential. Figure 4j and k respectively show that the electric field and potential of patterned materials processed by LDW and SSL change with time. We can see that the intensity and growth rate of electric field and potential of patterned materials processed by SSL are significantly higher than that of patterned materials processed by LDW. This further indicates that SSL synchronous excitation electrons have higher potential and electric field intensity. Electrode materials

possessing higher electric fields and potentials exhibit a stronger electrostatic attraction to charges and enhanced electrical conductivity. These attributes can be improved by modulating the electronic structure and inducing electronic/ion transfer at the electrode-electrolyte interface, thereby enhancing the charge transfer capabilities of the electrode material. This, in turn, facilitates charge diffusion and insertion, while reducing internal resistance, thereby enhancing electrochemical performance. Moreover, the increased capacity to adsorb a greater quantity of charge results in heightened energy density. Higher electric field intensities serve to expedite the adsorption and release of charges, consequently elevating the rate of charge and discharge, thereby achieving an enhancement in power density

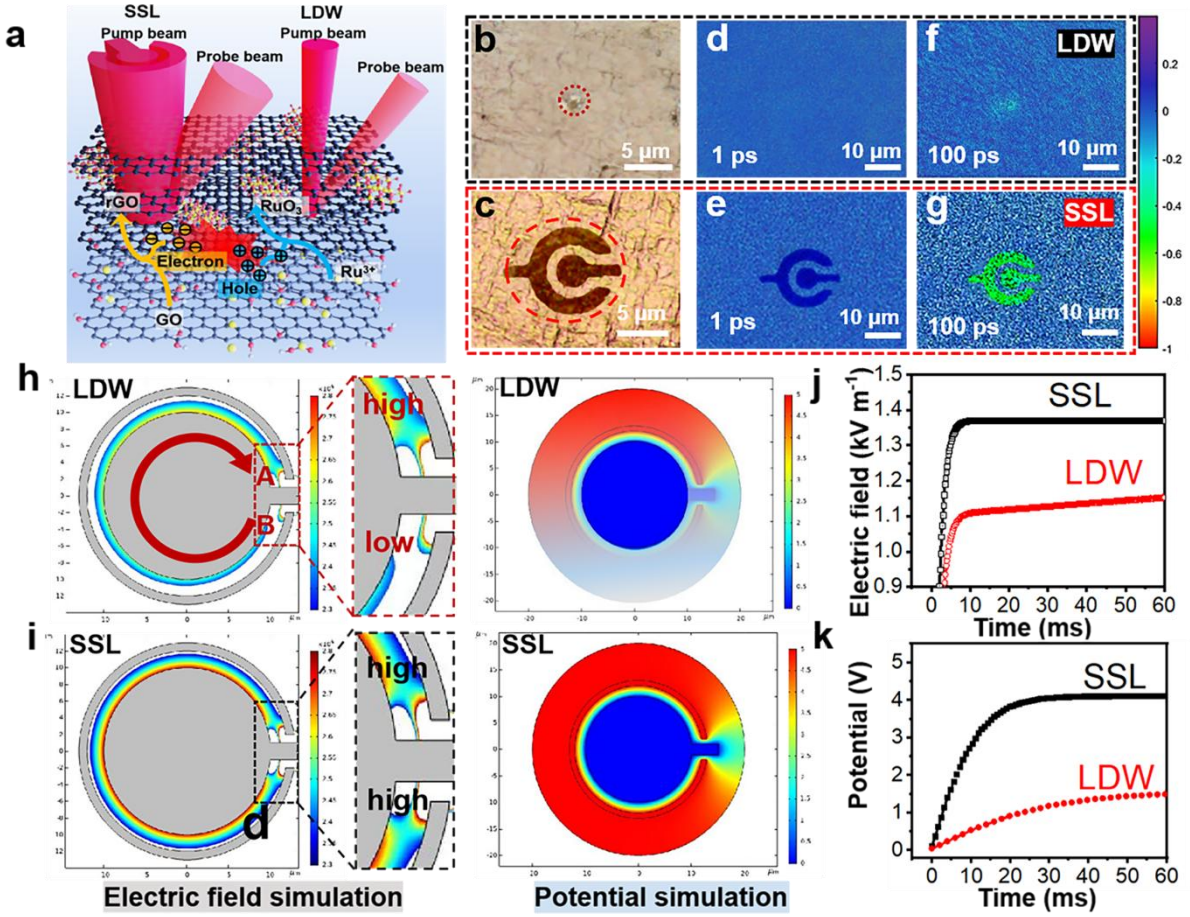

Figure 4. The results of pump probe and the simulation of the electric field and potential during SSL and LDW processing. (a) The schematic of pump probe by SSL and LDW ablation. (b) Optical image of the final structure during LDW processing. (c) Optical image of the final structure during SSL processing. (d)-(g) 2D mapping of the transient reflectivity at 1 ps and 100 ps delay times under irradiation of LDW and SSL. (h) and (i) The electric field and potential of LDW and SSF via COMSOL simulation. (j) The electric field varies with time during SSL and LDW processing. (k) The potential varies with time during SSL and LDW processing.

2.3 Electrochemical performance of MSCs with different electrode materials via SSL and LDW

As discussed previously, different laser pulse energies are designed to pattern and synthesize the mixed materials. According to the results of characterization test, it can be found that the photoinduced composites are different under different laser parameters. Therefore, the electrochemical properties of MSCs obtained under different laser pulse energies were tested. We varied the laser power (30-75 μW) of the SSL and LDW to investigate differences in conductivity of rGO/RuO_2-SSL and rGO/RuO_2-LDW electrodes. The resistance and conductivity of the material reached their minimum and maximum, respectively, when the laser power was 60 μW (Supplementary Figure 15). And we also find that the conductivity of rGO/RuO_2-SSL is always ahead of that of rGO/RuO_2-LDW. As shown in Supplementary Figure 16a, different Cyclic voltammograms curves (CVs) can directly reflect the difference in capacitance performance. Supplementary Figure 16b summarizes the areal capacitance obtained according to the CV diagrams. It can be concluded that the electrochemical performance is the highest when the laser pulse energy is 60 μW. In subsequent tests, we also selected the optimal parameters for detailed electrochemical tests.

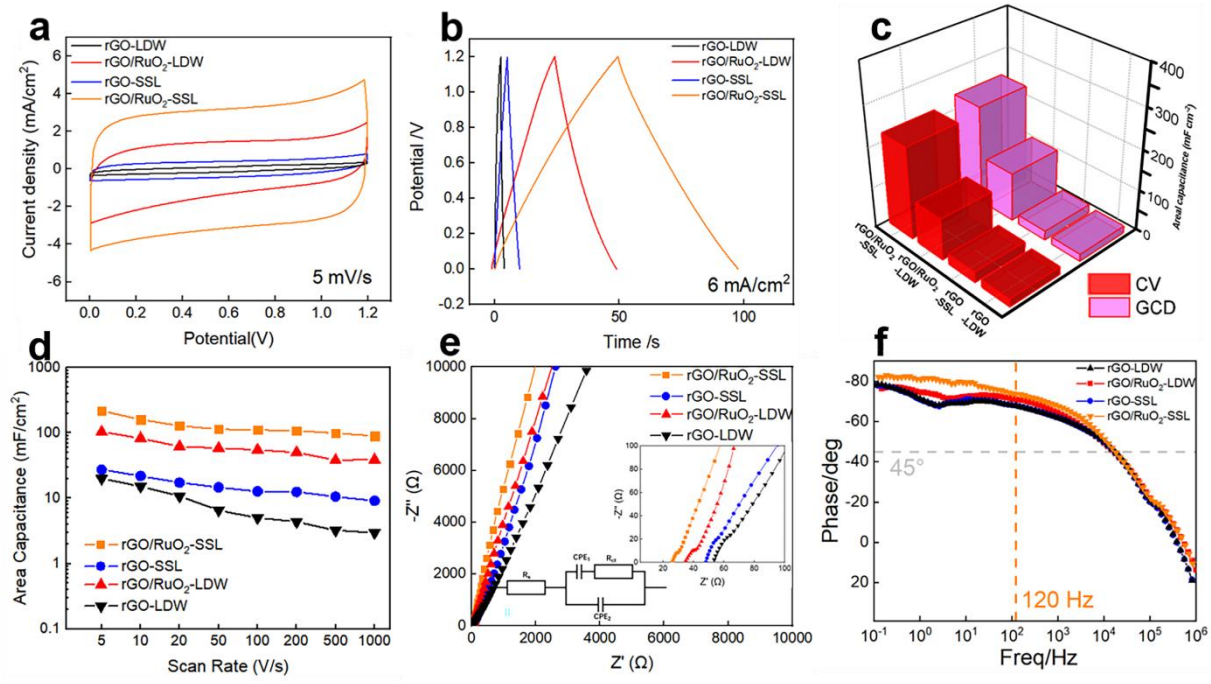

Figure 5. Electrochemical performances of different MSCs via SSL and LDW. (a) Cyclic voltammograms curves of rGO-SSL, rGO/RuO_2-SSL, rGO-LDW and rGO/RuO_2-LDW MSCs at a scan rate of 5 mV/s. (b) GCD cycle diagram of the different MSCs mentioned above at a current density of 6 mA cm^{-2}. (c) Electrochemical performance of electrode materials calculated from previous CV and GCD cycle diagrams (d) The areal capacitance of the rGO/RuO_2-SSL,

rGO-SSL, rGO/RuO_2-LDW and rGO-LDW MSCs calculated from CV curves under various scan rates. (e) Nyquist plots of the rGO/RuO_2-SSL, rGO-SSL, rGO/RuO_2-LDW and rGO-LDW MSCs. (f) Bode plots of the different MSCs.

After the preparation of rGO MSCs and rGO/RuO_2 MSCs via SSL and LDW, we focused on the electrochemical performance of the different electrode with 1 M Na_2SO_4 as the electrolyte. The charge storage behaviors of the electrodes were studied by CV and galvanostatic charge-discharge (GCD). Figure 5a shows the CV curves of rGO-SSL, rGO/RuO_2-SSL, rGO/RuO_2-LDW and rGO-LDW MSCs at a scan rate of 5 mV s^{-1}. It can be seen from the CV curves that the capacitance of the rGO/RuO_2-SSL MSC is significantly higher than that of the other MSCs. The nearly equilateral triangular like GCD curves at the current density of 6 mA cm^{-2} (Figure 5b). Figure 5c further demonstrate that the rGO/RuO_2-SSL MSC have excellent electrochemical performance compared with other MSCs. Figure 5d shows the areal capacitance of the MSCs calculated from CV curves under various scan rates, demonstrating the superior capacitance of the rGO/RuO_2-SSL MSC. The CV curves of rGO/RuO_2-SSL, rGO-SSL, rGO/RuO_2-LDW and rGO-LDW at scan rates ranging from 10 to 1000 mV/s are shown in Supplementary Figure 17. The reason why the capacitance performance of the rGO/RuO_2-LDW MSC is much smaller than that of the rGO/RuO_2-SSL MSC is that the RuO_2 as pseudocapacitive material, has a significantly higher capacitance than that of EDLC materials such as graphene. In contrast, the rGO/RuO_2-LDW MSC contains less RuO_2 nanoparticles due to the removal of rGO sheets by laser direct writing, thus the electrochemical performance is mainly dependent on the properties of rGO. As a conclusion, the SSL method ensures the consistency of the material and preserves the nanoporous structure of the reduced graphene oxide, which shortens the diffusion path of the electrolyte ions and facilitates fast ion transfer of charging/discharging process the good porous structure increases the contact area with the electrolyte, allowing the electrode materials to be fully exploited. Finally, the microns size of the MSCs prepared by SSL allows the electrolyte ions to transfer rapidly between electrodes, reducing the internal resistance and allowing the MSC to accomplish energy storage fleetly. The depiction in Figure 5e illustrates the equivalent circuit model, comprising capacitance elements CPE_1 and CPE_2, the interfacial charge-transfer resistance (Rct), and the bulk resistance (Rs). The Nyquist plots in Figure 5e of rGO/RuO_2-SSL, rGO/RuO_2-LDW, rGO-SSL, rGO-LDW MSCs exhibit distinct high-, mid-, and low-frequency regions, corresponding to electro-transfer-limited, diffusion-limited, and capacitive processes, respectively. The ESR encompasses the intrinsic electrode resistance, contact resistance with the current collector, and electrolyte resistance. The curve of rGO/RuO_2-SSL MSC shows an

almost vertical slope in the high frequency range compared to other MSCs, which indicates that the rGO/RuO_2-SSL MSC has desirable electrochemical properties. Due to the redox reaction between RuO_2 electrode material and electrolyte, a very small semicircle can be observed in the Nyquist plots. It is noteworthy that the Rs of the rGO/RuO_2-SSL (25 Ω) is comparatively lower when contrasted with those of the rGO/RuO_2-LDW, rGO-SSL, and rGO-LDW (38, 47, and 52 Ω, respectively). Furthermore, the Rct for rGO/RuO_2-SSL, rGO/RuO_2-LDW, rGO-SSL, and rGO-LDW is notably minimal, registering values of only 12.6, 18.7, 39.3, and 41.7 Ω, respectively.

These results confirm the low charge transfer resistance at the electrode/electrolyte interface and the rapid ions transfer in the redox reaction between electrode material and electrolyte. As shown in Figure 5f, the characteristic frequencies of the rGO-SSL, rGO/RuO_2-SSL, rGO-LDW and rGO/RuO_2-LDW MSCs at −45° are pretty close, around 37,000 Hz, corresponding to a time constant (τ0) of about 0.027 ms. This reflects the efficient ion transport/electron conductance. The MSCs had excellent capacitive behaviors, the phase angle at 120 Hz was measured to be 73.6°, 78.6° ,72.8° and 75.4°, corresponding to rGO-SSL, rGO/RuO_2-SSL, rGO-LDW and rGO/RuO_2-LDW MSCs, respectively. It can be found that rGO/RuO_2 MSCs are superior to other MSCs in various electrochemical performance indexes. In an exploration of Nyquist plots and Bode phase angle representations (as presented in Supplementary Figure 18 and 19) for the rGO/RuO_2-SSL composite, it becomes evident that the charge transfer resistance remains modest even subsequent to 10,000 charge/discharge cycles. Furthermore, the extensive duration of cycling tests does not introduce any discernible changes in the phase composition.

2.4 High electrochemical performance of rGO/RuO_2-SSL MSCs

After determining the optimal laser processing mode and laser pulse energy in advance, the parameters of electrode material thickness were also studied. As illustrated in Supplementary Figure 20, which portrays the SEM images of the cross-section of the initial GO/$RuCl_3$ hybrid films and the resulting rGO/RuO_2 film, we meticulously fabricated mixed films of GO/$RuCl_3$ with varying thicknesses. Notably, these films exhibited thickness measurements of 1, 2, 3, and 4 microns, respectively, all displaying well-defined layered structures that align with the typical structural attributes associated with two-dimensional materials. Notably, after undergoing laser processing, there is an observed increase in the film thickness. It is well known that under the same conditions, when our electrode material is thicker, its measured area ratio will be higher, because there is more accumulation of electrode

material per unit area. Therefore, when exploring the most suitable film thickness of our electrode material, we should consider both the areal and volumetric capacitance. As shown in Supplementary Figure 21a and b, CV curves and GCD profiles of MSCs under different film thicknesses were tested, and the areal and volumetric capacitance of MSCs under different thicknesses were calculated in Supplementary Figure 21c. In contrast, we found that both the areal and volumetric capacitance were superior when the film thickness was 3 microns. Therefore, in the subsequent electrochemical test, we choose the electrode material with this thickness for the test.

To further investigate the electrochemical performance of the rGO/RuO_2-SSL, we selected the optimal parameters from previous results to fabricate MSC. As shown in Figure 6a and Supplementary Figure 22, we tested the CV curves of the rGO/RuO_2-SSL MSCs at the sacn rates from 1~1000 mV s^{-1} under a voltage window of 1.2 V. Figure 6b shows the areal capacitance and volumetric capacitance under different scan rates. We obtained an areal capacitance of 516 mF cm^{-2} and a volumetric capacitance value of 1720 F cm^{-3} at a scan rate of 1 mV s^{-1}. Then, capacitance retention experiments were performed on our MSCs to further verify the electrochemical properties of the MSCs. The capacitance remained as high as 68.5% when the scan rate was increased from 20 to 2000 mV s^{-1} (Figure 6c). The GCD profiles were also obtained in Figure 6d and Supplementary Figure 23 at various current densities (0.5~10 mA cm^{-2}) under voltage windows of 1.2 V. The areal and volumetric capacitance of the rGO/RuO_2 MSC was concluded in Figure 6e. Figure 6f shows the capacitance retention of rGO/RuO_2 MSCs, with high capacitance (95%) retained and efficiency (98%) after 12,000 cycles, attributed to the stability of rGO as a carbon-based electrode material. Figure 6g and h show the CV and GCD curves of a single device, six devices in parallel and six devices in series. The MSCs exhibit excellent series and parallel electrochemical performance, capable of extending the voltage window up to 7V with six series devices and extending the charge and discharge times by a factor of six when connected in parallel. Supplementary Figure 24 and 25 show the SEM images of six MSCs in series and in parallel and multiple MSCs arrays combined. Supplementary Figure R26 provides an illustrative representation of the processing effects observed when numerous rGO/RuO_2-SSL MSCs are connected in a series configuration. Notably, the processing morphology of each individual rGO/RuO_2-SSL MSC exhibits a high degree of regularity. The depiction presented in Supplementary Figure 27 provides a visual representation of rGO/RuO_2-SSL MSCs, which is observed to power the light-emitting diode (LED) and a miniature calculator.

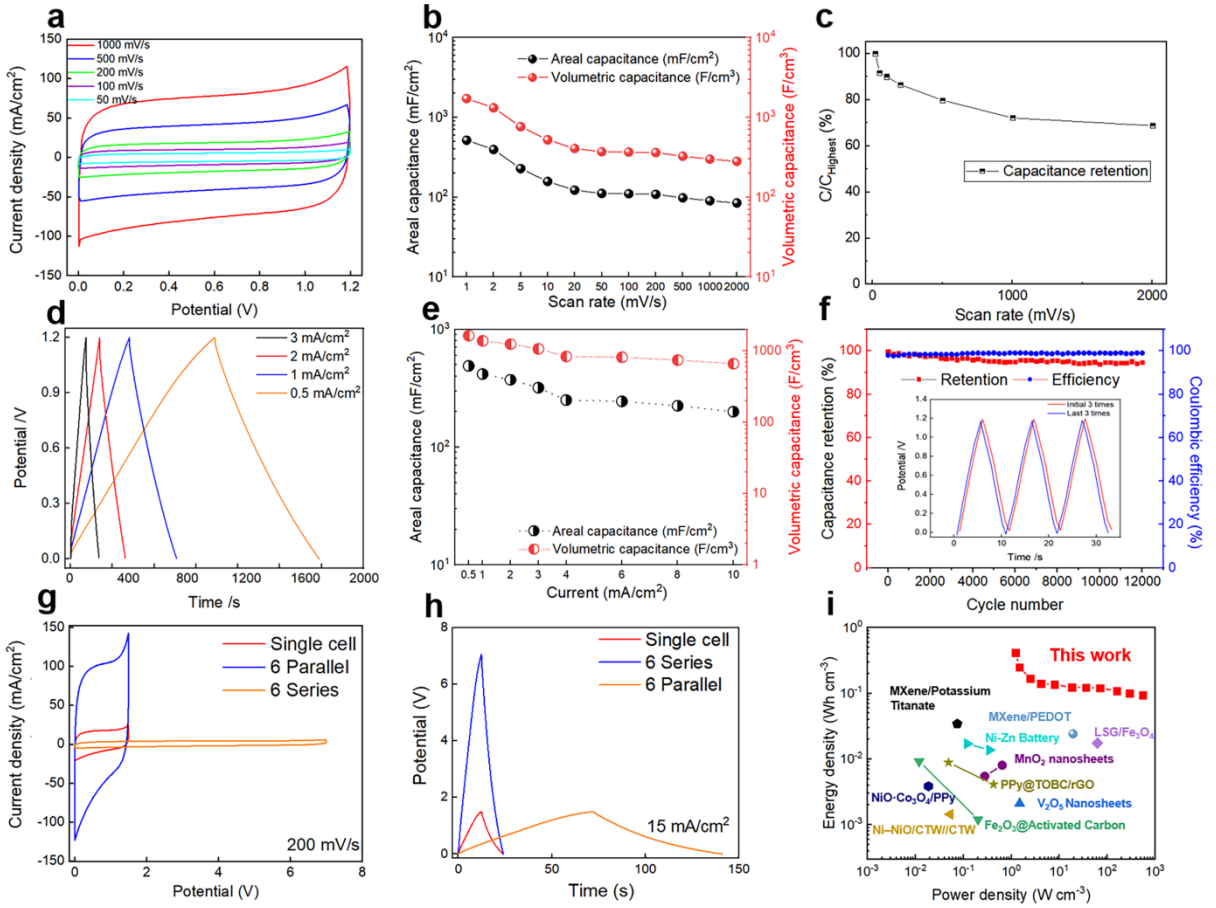

Figure 6. Electrochemical performance of rGO/RuO_2-SSL MSCs with optimal performance. (a) CV curves of rGO/RuO_2-SSL MSCs at various scan rates. (b) The areal capacitance and volumetric capacitance under different scan rates. (c) The capacitance remained of the rGO/RuO_2-SSL MSCs. (d) GCD profiles of rGO/RuO_2 MSCs from 0.5 to 3 mA cm^{-2}. (e) The areal capacitance and volumetric capacitance under different current densities. (f) The retention and efficiency of the MSCs after 12,000 cycles. Inset: the first and last three cycles. (g) CV curves of a single device, six devices in parallel and six devices in series. (h) GCD profiles of a single device, six devices in parallel and six devices in series. (i) Energy and power densities of the rGO/RuO_2-SSL MSCs compared with other capacitors.

According to the energy density equation $E= CV^2/2$, where E represents the energy density of the MSC, C represents the capacitance of the MSC and V represents the operating voltage window. It is clear from the equation that the voltage window plays an important role in the energy storage. Although the electrolytic voltage of water is 1.23 V, the lower concentration of hydrogen and hydroxide ions in the neutral electrolyte allows for an increased gas evolution voltage. At the same time, the nanostructure of rGO has a large specific surface area and can provide an ion diffusion channel for RuO_2 nanoparticles attached to the rGO lamella, which is conducive to the rapid transport of hydrogen ions. Figure 6i shows energy densities and power

densities of the rGO/RuO_2 MSCs compared with other supercapacitors. The rGO/RuO_2 MSCs demonstrate an extremely superior volumetric energy density of 0.41 Wh cm^{-3} and an excellent volumetric power density of 568 W cm^{-3}, much higher than other MSCs presented in previous studies.[43-51] In order to underscore our superior performance, we have compiled a set of analogous works in Supplementary Table 1, wherein we conduct a comparative analysis of performance parameters, encompassing capacitance, energy density, and power density. Evidently, our results stand at the forefront, underscoring our exceptional performance advantage.

3. Conclusion

In conclusion, our technology presents an expedited, single-step method for the preparation of micron-sized supercapacitors. This approach effectively surmounts the hurdles associated with material removal and low efficiency encountered in LDW techniques. Moreover, it enables in situ photochemical synthesis of composite electrode materials with better performance by bringing higher electric field and potential through laser-induced electron synchronization excitation. We have provided a comprehensive explanation for the superiority of our SSL technique over LDW in terms of both patterning and photochemical synthesis. The result SSL-MSCs have extremely high capacitance (516 mF cm^{-2} and 1720 F cm^{-3}), good cycle life (95% after 12,000 cycles) and ultra-high energy density and power density (0.41 Wh cm^{-3} and 568 W cm^{-3}). This strategy provides valuable insights for the design of the structural and electrode materials of the next generation of MSCs and their integrated applications.

4. Experimental Section

GO/$RuCl_3$ films preparation. The GO dispersion (2 mg/mL, 50-200nm) was purchased from XFNANO, Inc. (Nanjing, China) and the ruthenium chloride powder was purchased from InnoChem, Ltd. (Beijing, China). The ruthenium chloride powder (3 mg) was dispersed in deionised water (15 mL). The GO dispersion (1.5 mL) was mixed with the $RuCl_3$ aqueous solution and sonicated for 2 h. The prepared mixture was filtered under vacuum. The nitrocellulose membranes used for vacuum filtration were purchased from Merck Millipore Ltd. (Tullagreen, Ireland). Vacuum filtration was carried out for approximately 2 h to obtain mixed films of GO/$RuCl_3$, which was then vacuum dried. After dissolving the filtered membrane with acetone solution, GO/$RuCl_3$ hybrid membranes were obtained and the films were transferred onto Si substrates.

Laser direct writing process: Ti: sapphire laser system was used to emit femtosecond laser

pulses with 35 fs pulse duration, 800 nm wavelength and 1 kHz repetition rate. The femtosecond laser beam is focused by a 20×Olympus microscope objective (NA = 0.45) and the laser beam scans at a speed of 3000 um/s.

Spatially shaped laser process: Using a spatial light modulator (Holoeye Pluto, SLM), the Gaussian beam can be shaped into an arbitrary pattern of light fields. We transform the designed MSC shape into a phase grey scale map with a certain number of pixels. The spatial light modulator can load the phase difference distribution and reflect the laser beam out. We used the improved Gerchberg–Saxton algorithm to optimise the gray-scale phase holograms. The light field transformation for arbitrary geometries is then achieved by loading the phase difference distribution onto the SLM.

Characterization of rGO/RuO_2 MSCs: Optical microscopy images were obtained by Olympus metallographic microscope. Scanning electron microscope (SEM) images were taken by SU8220 (Hitachi, Japan) SEM. Transmission electron microscope (TEM) images were collected on JEM-2100 TEM. X-ray photoelectron spectroscopy (XPS) spectra was obtained on a PHI Quantera spectrometer (ULVAC-PHI, Japan). The Raman spectra were obtained using a Renishaw inVia Reflex spectrometer.

Electrochemical characterizations of MSCs: Cyclic voltammogram (CV), galvanostatic charge-discharge (GCD), and electrochemical impedance spectra (EIS) were measured by CHI760D electrochemical workstation, using 1M Na_2SO_4 electrolyte. The MSCs were connected with a Probe Station (MPS-100S) by tungsten probes (tip 1 um) to obtain the electrochemical characterizations. The specific capacitance (C) of MSCs were calculated from the CV and GCD curves by using Eqs. (1) and (2):

$$C = \frac{1}{\vartheta \times V} \int_{Vi}^{Vf} I(V) dV \tag{1}$$

where I, ϑ, and V represent the current applied, scanning rate, and voltage (Vf and Vi are the final voltage and initial voltage).

$$C = \frac{I}{(-dV / dt)} \tag{2}$$

The discharge current is represented by I, and the slope of the discharge curve is denoted as dV/dt. To assess the cycling stability of the supercapacitors, a series of constant current charge-discharge cycles were performed at a rate of 1 mA for 15,000 cycles. To calculate the energy densities (mWh cm^{-2}) of the supercapacitors, the following equations were employed, where

ΔE represents the operating voltage window:

$$E_{cell} = C_{cell}\Delta E^2 /(2\times 3{,}600) \tag{3}$$

where I is the discharge current, and dV/dt is the slope of the discharge curve. Cycling stability measurements were performed by repeating constant current charge-discharge at 1 mA for 15,000 cycles. The energy densities (μWh cm^{-2}) of the supercapacitors were calculated according to the following equations:

$$P_{cell} = E_{cell}\times 3{,}600/t \tag{4}$$

where t represents the discharge time ($t = \Delta V/\vartheta$).

Declaration of Competing Interest

The authors declare that they have no known competing financial interests or personal relationships that could have influenced the work reported in this paper.

Acknowledgments

This research was supported by National Key R&D Program of China (Grant No. 2022YFB4600400), Key projects of the Natural Science Foundation of China (Grant No. 52235009), the National Natural Science Foundation of China (NSFC) (Grant No. 52275401) and Beijing Institute of Technology Science and Technology Innovation Program (Grant No. 2022CX01018).

References

[1] B. D. Gates, Flexible electronics. *Science* **2009**, 323, 1566–1567.

[2] J. A. Rogers, T. Someya, Y. G. Huang, Materials and mechanics for stretchable electronics. *Science* **2010**, 327, 1603–1607.

[3] W. Gao, S. Emaminejad, H. Y. Y. Nyein, S. Challa, K. Chen, A. Peck, H. M. Fahad, H. Ota, H. Shiraki, D. Kiriya, D. Lien, G. Brooks, R. W. Davis, A. Javey, Fully integrated wearable sensor arrays for multiplexed in situ perspiration analysis. *Nature* **2016**, 529, 509–514.

[4] J. Chmiola, C. Largeot, P. L. Taberna, P. Simon, Y. Gogotsi, Monolithic carbide-derived carbon films for micro-supercapacitors. *Science* **2010**, 328, 480–483.

[5] N. A. Kyerematen, T. Brousse, D. Pech, Microsupercapacitors as miniaturized energy-

storage components for on-chip electronics. *Nat. Nanotechnol.* **2017**, 12, 7-15.

[6] A. González, E. Goikolea, J. A. Barrena, R. Mysyk, Review on supercapacitors: Technologies and material. *Renew. Sust. Energ. Rev.* **2016**, 58, 1189-1206.

[7] Y. Wang, Y. Xia, Recent progress in supercapacitors: from materials design to system construction. *Adv. Mater.* **2013**, 25, 5336-5342.

[8] N. Liu, Y. Gao, Recent progress in micro-supercapacitors with in-plane interdigital electrode architecture. *Small*, **2017**, 13, 1701989.

[9] J. Ren, L. Li, C. Chen, X. Chen, Z, Cai, L. Qiu, Y. Wang, X. Zhu, H. Peng, Twisting carbon nanotube fibers for both wire-shaped micro-supercapacitor and micro-battery. *Adv. Mater.* **2013**, 25, 1155-1159.

[10] A. Paul, S. Ghosh, H. Kolya, C. Kang, N. C. Murmu, T. Kuila. New insight into the effect of oxygen vacancies on electrochemical performance of nickel-tin oxide/reduced graphene oxide composite for asymmetric supercapacitor. *J Energy Storage* **2023**, 62, 106922.

[11] R. B. Chrisma, R. I. Jafri, E. I. Anila. A review on the electrochemical behavior of graphene–transition metal oxide nanocomposites for energy storage applications. *J. Mater. Sci.* **2023**, 58, 6124-6150.

[12] V. Molahalli, V. S. Bhat, A. Shetty, D. Hundekal, A. Toghan, G. Hegde. ZnO doped SnO_2 nano flower decorated on graphene oxide/polypyrrole nanotubes for symmetric supercapacitor applications. *J Energy Storage* **2023**, 69, 107953.

[13] M. Miah, P. Hota, T. K. Mondal, R. Chen, S. K. Saha. Mixed metal sulfides ($FeNiS_2$) nanosheets decorated reduced graphene oxide for efficient electrode materials for supercapacitors. *J. Alloys Compd.* **2023**, 933, 167648.

[14] G. K. Maron, M.G. Masteghin, V. Gehrke, L. S. Rodrigues, J. Alano, J. H.H. Rossato, V. R. Mastelaro, J. Dupont, M. T. Escote, S. R. P. Silva, N. L. V. Carreno. Enhanced pseudocapacitive behaviour in laser-written graphene micro-supercapacitors decorated with nickel cobalt sulphide nanoparticles. *Mater. Res. Bull.* **2023**, 168, 112490.

[15] Z. Ai, L. Li, M. Huang, X. Su, Y. Gao, J. Wu. An Ultrafast, High-Loading, and Durable Poly (p-aminoazobenzene)/Reduced Graphene Oxide Composite Electrode for Supercapacitors. *Adv. Funct. Mater.* **2023**, 33, 2211057.

[16] L. Li, L. Yu, C. Guo, X. Xiong, F. Fan, W. Yang, F. She, C. He. Green Fabrication of Agglomeration-Reductive and Electrochemical-Active Reduced Graphene Oxide/Polymerized Proanthocyanidins Electrode for High-Performance Supercapacitor. *ACS Appl. Energy Mater.* **2023**, 1, 369-379.

[17] Y. Yuan, L. Jiang, X. Li, P. Zuo, C. Xu, M. Tian, X. Zhang, S. Wang, B. Lu, C. Shao, B.

Zhao, J. Zhang, L. Qu, T. Cui, Laser photonic-reduction stamping for graphene-based micro-supercapacitors ultrafast fabrication. *Nat. Commun.* **2020**, 11, 6185.

[18] E. Lim, C. Jo, M. S. Kim, M. H. Kim, J. Chun, H. Kim, J. Park, K. C. Roh, K. Kang, S. Yoon, J. Lee, High-Performance Sodium-Ion Hybrid Supercapacitor Based on Nb_2O_5 @Carbon Core-Shell Nanoparticles and Reduced Graphene Oxide Nanocomposites. *Adv. Funct. Mater.* **2016**, 26, 3711–3719.

[19] Z .L. Jian, V. Raju, Z. F. Li, Z. Y. Xing, Y. S. Hu, X. L. Ji, A High-Power Symmetric Na-Ion Pseudocapacitor. *Adv. Funct. Mater.* **2015**, 25, 5778–5785.

[20] Q. Jiang, N. Kurra, M. Alhabeb, Y. Gogotsi, H. N. Alshareef, All pseudocapacitive MXene-RuO_2 asymmetric supercapacitors. *Adv. Energy Mater.* 2018, 8, 1703043.

[21] H. Ma, D. Kong, Y. Xu, X. Xie, Y. Tao, Z. Xiao, W. Lv, H. D. Jang, J. Huang, Q. H. Yang, Disassembly–reassembly approach to RuO_2/graphene composites for ultrahigh volumetric capacitance supercapacitor. *Small* **2017**, 13, 1701026.

[22] F. Karimi, S. Korkmaz, C. Karaman, O. Karaman, A. Kariper, Engineering of GO/MWCNT/RuO_2 ternary aerogel for high-performance supercapacitor. *Fuel* **2022**, 329, 125398.

[23] H. Wang, L. Tian, M. Ali, X. Zhao, S. Han, Z. Xing. Two-step electrodeposition synthesis of $NiCo_2S_4$/MoS_x composite on nickel foam as electrodes for supercapacitors. *J. Alloys Compd.* **2023**, 932, 167628.

[24] M. Xiao, M. Xiao, S. Yang, W. Zhang, X. Niu, X. Du, X. Hui. Enhancement of electrochemical properties of electrodes for high performance supercapacitors by electrodeposition of CoSe on hydrothermally prepared $CuCo_2O_4$. *J. Alloys Compd.* **2023,** 172199.

[25] MZU. Shah, H. Hou, M. Sajjad, MS. Shah, K. Safeen, A. ShahShah. Iron-selenide-based titanium dioxide nanocomposites as a novel electrode material for asymmetric supercapacitors operating at 2.3 V. *Nanoscale Adv.* **2023**, 5, 1465-1477.

[26] E. Bertran-Serra, A. Musheghyan-Avetisyan, S. Chaitoglou, R. Amade-Rovira, I. Alshaikh, F. Pantoja-Suárez, J. Andújar-Bella, T. Jawhari, A. Perez-del-Pino, E. Gyorgy. Temperature-modulated synthesis of vertically oriented atomic bilayer graphene nanowalls grown on stainless steel by inductively coupled plasma chemical vapour deposition. *Appl. Surf. Sci.* **2023**, 610, 155530.

[27] HY. Ho, HI. Chu, YJ. Huang, DS. Tsai, CP. Lee. Polypyrrole-coated copper@ graphene core-shell nanoparticles for supercapacitor application. *Nanotechnology* **2023**, 34, 125401.

[28] Y. Rao, M. Yuan, B. Gao, L. Hui, J. Yu, X. Chen, Laser-scribed phosphorus-doped

graphene derived from Kevlar textile for enhanced wearable micro-supercapacitor. *J. Colloid Interface Sci.* **2023**, 630, 586-594.

[29] G. Yuan, T. Wan, A. BaQais, Y. Mu, D. Cui, M. A. Amin, X. Li, B. B. Xu, X. Zhu, H. Algadi, H. Li, P. Wasnik, N. Lu, Z. Guo, H. Wei, B. Cheng. Boron and fluorine Co-doped laser-induced graphene towards high-performance micro-supercapacitors. *Carbon* **2023**, 212, 118101.

[30] W. Wang, L. Xu, L. Zhang, A. Zhang, J. Zhang. Self-Powered Integrated Sensing System with In-Plane Micro-Supercapacitors for Wearable Electronics. *Small* **2023**, 2207723.

[31] L. Jiang, A. D. Wang, B. Li, T. H. Cui, Y. F. Lu, Electrons dynamics control by shaping femtosecond laser pulses in micro/nanofabrication: modeling, method, measurement and application. *Light Sci. Appl.* **2018**, 7, 17134.

[32] Y. Yuan, L. Jiang, X. Li, P. Zuo, X. Zhang, Y. Lian, Y. Ma, M. Liang, Y. Zhao, L. Qu, Ultrafast Shaped Laser Induced Synthesis of MXene Quantum Dots/Graphene for Transparent Supercapacitors. *Adv. Mater.* **2022**, 34, 2110013.

[33] Y. Yuan, Z. Zhang, X. Li, L. Jiang, X. Zhang, P. Zuo, C. Xu, L. Ma, S. Wang, Y. Zhao, L. Qu, Bottom-up scalable temporally-shaped femtosecond laser deposition of hierarchical porous carbon for ultrahigh-rate micro-supercapacitor. *Sci. China Mater.* **2022**, 65, 2412-2420.

[34] V. D. Patake, C. D. Lokhande, Chemical synthesis of nano-porous ruthenium oxide (RuO_2) thin films for supercapacitor application. *Appl. Surf. Sci.* **2008**, 254, 2820-2824.

[35] H. Xia, Y. S. Meng, G. Yuan, C. Cui, L. Lu, A symmetric RuO_2/RuO_2 supercapacitor operating at 1.6 V by using a neutral aqueous electrolyte. *ECS Solid State Lett.* **2012**, 15, A60.

[36] Z. Sun, Z. Liu, B. Han, S. Miao, J. Du, Z. Miao, Microstructural and electrochemical characterization of RuO2/CNT composites synthesized in supercritical diethyl amine. *Carbon* **2006**, 44, 888-893.

[37] Y. Wang, X. Zhang, Preparation and electrochemical capacitance of RuO_2/TiO_2 nanotubes composites. *Electrochim. Acta* **2004**, 49, 1957-1962.

[38] W. Q. Li, R. Y. Zhou, X. T. Wang, L. Y. Hu, X. Chen, P. C. Guan, X.G. Zhang, H. Zhang, J. C. Dong, Z. Q. Tian, J. F. Li, Identification of the molecular pathways of RuO_2 electroreduction by in-situ electrochemical surface-enhanced Raman spectroscopy. *J Catal* **2021**, 400, 367-371.

[39] S. Ramesh, K. Karuppasamy, A. Sivasamy, H. S. Kim, H. M. Yadav, H. S. Kim, Core shell nanostructured of Co_3O_4@ RuO_2 assembled on nitrogen-doped graphene sheets electrode for an efficient supercapacitor application. *J. Alloys Compd.* **2021**, 877, 160297.

[40] Y. Gao, D. Zheng, Q. Li, W. Xiao, T. Ma, Y. Fu, Z. Wu, L. Wang, 3D Co_3O_4-RuO_2 Hollow

Spheres with Abundant Interfaces as Advanced Trifunctional Electrocatalyst for Water-Splitting and Flexible Zn–Air Battery. *Adv. Funct. Mater.* **2022**, 32, 2203206.

[41] Q. Yao, Z. Yu, Y. H. Chu, R. S. Chan, Y. Xu, Q. Shao, X. Huang, S incorporated RuO_2-based nanorings for active and stable water oxidation in acid. *Nano Res*. **2022**, 15, 3964-3970.

[42] X. Lin, Z. Zhou, Q. Y. Li, D. Xu, S. Y. Xia, B. L. Leng, G. Y. Zhai, S. N. Zhang, L. H. Sun, G. Zhao, J. S. Chen, X. H. Li, Direct Oxygen Transfer from H_2O to Cyclooctene over Electron-Rich RuO_2 Nanocrystals for Epoxidation and Hydrogen Evolution. *Angew. Chem. Int. Ed.* **2022**, 134, e202207108.

[43] L. Qin, Q. Tao, A. E. Ghazaly, J. Fernandez-Rodriguez, P. O. Å. Persson, J. Rosen, F. Zhang, High-performance ultrathin flexible solid-state supercapacitors based on solution processable $Mo_{1.33}C$ MXene and PEDOT: PSS. *Adv. Funct. Mater.* **2018**, 28, 1703808.

[44] S. Zheng, J. Ma, K. Fang, S.Li, J. Qin, Y.Li, J. Wang, L. Zhang, F. Zhou, F Liu, K. Wang, Z. Wu, High-Voltage Potassium Ion Micro-Supercapacitors with Extraordinary Volumetric Energy Density for Wearable Pressure Sensor System. *Adv. Energy Mater.* **2021**, 11, 2003835.

[45] L. Li, R. Xiao, X. Tao, Y. Wu, L. Jiang, Z. Zhang, Y. Qing, Free-standing electrodes via coupling nanostructured Ni–NiO with hierarchical wood carbon for high-performance supercapacitors and Ni–Zn batteries. *J. Power Sources* **2021**, 491, 229618.

[46] Z. H. Huang, Y. Song, D. Y. Feng, Z. Sun, X. Sun, X. X. Liu, High mass loading MnO_2 with hierarchical nanostructures for supercapacitors. *ACS nano* **2018**, 12, 3557-3567.

[47] J. Wen, B. Xu, J. Zhou, Y. Chen, Novel high-performance asymmetric supercapacitors based on nickel-cobalt composite and PPy for flexible and wearable energy storage. *J. Power Sources* **2018**, 402, 91-98.

[48] N. Sheng, S. Chen, J. Yao, F. Guan, M. Zhang, B. Wang, Z. Wu, P. Ji, H. Wang, Polypyrrole@ TEMPO-oxidized bacterial cellulose/reduced graphene oxide macrofibers for flexible all-solid-state supercapacitors. *Chem. Eng. J.* **2019**, 368, 1022-1032.

[49] J. Li, Y. Wang, W. Xu, Y. Wang, B. Zhang, S. Luo, X. Zhou, C. Zhang, X. Gu, C. Hu, Porous Fe_2O_3 nanospheres anchored on activated carbon cloth for high-performance symmetric supercapacitors. *Nano Energy* **2019**, 57, 379-387.

[50] L. Hua, Z. Ma, P. Shi, L. Li, K. Rui, J. Zhou, X. Huang, X. Liu, J. Zhu, G. Sun, W. Huang, Ultrathin and large-sized vanadium oxide nanosheets mildly prepared at room temperature for high performance fiber-based supercapacitors. *J. Mater. Chem. A* **2017**, 5, 2483-2487.

[51] L. Li, R. Xiao, Y. Wu, L. Jiang, Z. Zhang, Y. Qing, Free-standing electrodes via coupling nanostructured Ni–NiO with hierarchical wood carbon for high-performance supercapacitors and Ni–Zn batteries. *J. Power Sources* **2021**, 491, 229618.

TOC

This work proposes a novel approach for synthesizing and patterning composite electrodes using multi-point electron synchronization excitation. It not only significantly enhances the processing efficiency for MSCs and the quality of electrode materials but also circumvents the influence of electrode morphology during the traditional laser direct writing. This strategy leads to the better production of electrode materials exhibiting enhanced electrochemical performance and provides a means to achieve better efficiency and quality in the fabrication of MSCs.

Laser-induced Electron Synchronization Excitation for Photochemical Synthesis and Patterning Graphene-based Electrode

Yongjiu Yuan[a,b,c,d], *Junhao Huang*[a,b,c], *Xin Li*[*,a,b,c], *Lan Jiang*[a,b,c], *Tong Li*[d], *Pengcheng Sun*[d], *Yingying Yin*[d], *Sumei Wang*[a,b,c], *Qian Cheng*[a,b,c], *Wanghuai Xu*[d,e], *Liangti Qu*[f], *Steven Wang*[d]

a. Laser Micro/Nano-Fabrication Laboratory, School of Mechanical Engineering, Beijing Institute of Technology, Beijing, P. R. China.

b. Yangtze Delta Region Academy of Beijing Institute of Technology, Jiaxing, P. R. China.

c. Beijing Institute of Technology Chongqing Innovation Center, Chongqing, P. R. China.

d. Department of Mechanical Engineering, City University of Hong Kong, Hong Kong, P.R. China.

e. MOE Key Laboratory of Bioorganic Phosphorus Chemistry & Chemical Biology, Department of Chemistry, Tsinghua University, Beijing, P. R. China.